OPEN ACCESS

Effective medium multipolar tensor analysis of second-harmonic generation from metal nanoparticles

To cite this article: Mariusz Zdanowicz *et al* 2011 *New J. Phys.* **13** 023025

View the article online for updates and enhancements.

Effective medium multipolar tensor analysis of second-harmonic generation from metal nanoparticles

Mariusz Zdanowicz[1,2,4], **Sami Kujala**[1,3], **Hannu Husu**[1]
and Martti Kauranen[1]

[1] Department of Physics, Optics Laboratory, Tampere University of Technology, PO Box 692, FI-33101 Tampere, Finland
[2] Department of Transmission and Optical Technology, National Institute of Telecommunications, Szachowa Str. 1, 04-894 Warsaw, Poland
E-mail: mariusz.zdanowicz@tut.fi

Abstract. We present a detailed multipolar tensor analysis of second-harmonic (SH) generation from arrays of L-shaped gold nanoparticles. We define three effective nonlinear tensors, which include electric dipoles only (A^{eee}) and lowest-order magnetic (and quadrupole) effects at the fundamental (A^{eem}) and the SH (A^{mee}) frequency. The components of the various tensors are distinguished through their different transformations as the experimental geometry is varied. The response is dominated by electric-dipole effects. However, the higher multipoles also play a significant role and are more important at the fundamental frequency than at the SH frequency. The results correlate well with the particles' plasmonic resonances and symmetry rules.

[3] Current address: Department of Micro and Nanosciences, Aalto University School of Science and Technology, PO Box 13500, FI-00076 Aalto, Finland
[4] Author to whom any correspondence should be addressed.

IOP Institute of Physics ◆ DEUTSCHE PHYSIKALISCHE GESELLSCHAFT

Contents

1. Introduction

The optical properties of metal nanostructures are dominated by the collective oscillations of conduction electrons, giving rise to plasmon resonances [1]. These resonances depend on the particle size and shape as well as their number and mutual ordering when they are organized in arrays. The resonances can lead to strong enhancement of the local electromagnetic fields within the structure [2]–[6]. Such strong local fields may enhance the optical responses of the structure, especially the nonlinear ones, which scale with the high power of the local field.

The local material properties and electromagnetic fields in nanostructures thus exhibit strong nanoscale variations. Such gradients may be favorable for higher-multipole interactions [7], thereby making magnetic dipoles, electric quadrupoles, etc important in the optical responses. The standard electric-dipole approximation may thus not be sufficient to describe the optical responses of nanostructures. In fact, two different types of multipoles should be taken into account [8]–[10]: those corresponding to microscopic multipole moments, arising from the atomic-scale light–matter interaction Hamiltonian [11], and those related to Mie scattering theory [1, 12], where the atomic-scale interaction may be of the electric-dipole origin, and the multipole effects arise from field retardation effects over the nanostructure. However, the radiation patterns of both types are similar in the far field. Moreover, there are particular challenges regarding the understanding of the role of different multipolar interactions in the nonlinear optical responses of various types of samples [13]–[16].

A number of works have addressed the role multipole effects in the optical responses of various kinds of nanoparticles [17]–[20]. Krenn *et al* [21] provided experimental evidence of multipolar plasmon resonances from elongated silver nanoparticles, where resonances depend on the nanoparticle length. The magnetic resonances are thought to play an important role in the properties of metamaterials [22]; however, the role of electric quadrupole effects has also recently been emphasized [23]. The nonlinear properties of nanoparticles as well as the multipolar contributions to the nonlinear properties are a subject of increasing interest [8]–[10], [24]–[27]. Second-harmonic generation (SHG) from arrays of split-ring resonators (SRRs) was studied by Klein *et al* [22]. They found that SHG was the most efficient when the magnetic resonance of the structure was excited. In addition, Petschulat *et al* [28] present a new analytical approach to the nonlinear properties of SRRs). They use a self-consistent model that describes the linear response of meta-atom geometries by their intrinsic plasmonic eigenmodes and includes multipolar effects. The simulated results were then used to estimate the nonlinear interactions that include the expected enhanced SH signal due to both electric and magnetic resonances. In addition, dipolar and quadrupolar effects have been shown

to play an important role in incoherent second-harmonic (SH) scattering from nanoparticles, both in ensemble [11, 27, 29] and single-particle measurements [8].

We have recently provided evidence of significant multipole interference in coherent SH emission from arrays of gold nanoparticles. Our approach [30, 31] was based on the differences between the fundamental radiative properties of electric dipoles as opposed to magnetic dipoles and electric quadrupoles [32]. The higher multipoles were estimated to contribute up to 20% of the total emitted SH field amplitude. Moreover, the tensor components forbidden for the ideal symmetry of the particles were found to play an important role in the SH response of the system [31]. This fact was explained by the chiral symmetry breaking of the particles, giving rise to the dipolar and effective quadrupolar sources that would be forbidden for the case of ideal particles. In this interpretation, the role of surface defects is particularly important, because they can act as local sources of SHG with retardation between the sources giving rise to effective quadrupoles. However, the measurement technique used is only able to provide evidence of higher-multipole interactions at the SH frequency.

In this paper, we extend our experimental approach further by defining effective nonlinear tensors for the nanostructure that include electric and magnetic effects at the fundamental and SH frequencies. Our magnetic tensors also account for the electric quadrupoles, because on the basis of present knowledge, the two types of effects cannot be separated from each other in the measured coherent SHG signals [33]. By relying on the different transformation properties of the nonlinear tensors as the experimental geometry is varied, we provide evidence of higher-multipole interactions at both the fundamental and the SH frequency. In particular, we find that for the structures investigated, the higher multipole effects are even stronger at the fundamental frequency than at the SH frequency.

2. Theoretical basis

The traditional model of the nonlinear response based on the electric-dipole approximation and the nonlinear susceptibility is not well suited to describing the nonlinear responses from metal nanostructures. This is because the local fields and material properties, such as the susceptibility, exhibit strong spatial variations in the scale of a wavelength or less. A full description of such effects is computationally extremely demanding and has been done only for some simple model cases [8, 9, 12, 34]. To avoid such nanoscale difficulties, we have introduced a macroscopic nonlinear response tensor (NRT) approach, in which the sample is treated as a 'black box', and the interesting quantities are the input and output radiation fields [35]. In our earlier implementation of this approach, the structure of the NRT was determined by electric-dipole-type symmetry rules for a given experimental situation at a time. With this limitation in mind, the NRT can also be considered as equivalent to the nonlinear susceptibility tensor in the effective medium limit of the sample.

In this paper, we extend the NRT approach to account for dipole and higher-multipole interactions. Up to lowest-order magnetic-dipole and electric-quadrupole effects, the effective SH source polarization, magnetization and quadrupolarization are [33, 36]

$$P_i(2\omega) = A_{ijk}^{eee}(2\omega, \omega, \omega)E_j(\omega)E_k(\omega) + A_{ijk}^{eem}E_j(\omega)B_k(\omega) + A_{ijkl}^{eeQ}E_j(\omega)\nabla_k E_l(\omega), \tag{1}$$

$$M_i(2\omega) = A_{ijk}^{mee}(2\omega, \omega, \omega)E_j(\omega)E_k(\omega), \tag{2}$$

$$Q_{ij}(2\omega) = A_{ijkl}^{Qee}(2\omega, \omega, \omega)E_k(\omega)E_l(\omega), \tag{3}$$
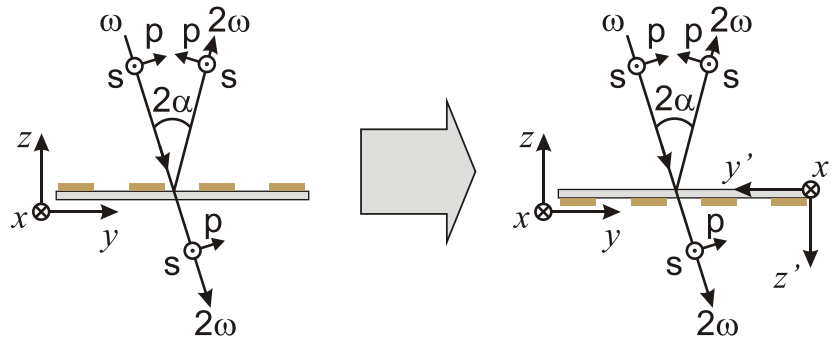
Figure 1. The geometry of the measurements: the fundamental beam is first incident on the metal side of the sample and after flipping the sample over on the substrate side. The angle of incidence α is kept relatively small ($<1°$), which allows us to identify s- and p-polarizations with x- and y-polarizations, respectively. After flipping the sample, the coordinate system connected with the sample is transformed with respect to the laboratory coordinate system with $x = x'$; $y = -y'$; $z = z'$.

respectively, and the indices i, j and k refer to Cartesian field components. In addition, emission from the quadrupolarization involves a gradient of the source with respect to the direction of emission $\nabla_i Q_{ij}$ [32].

The present understanding, however, is that magnetic-dipole and electric-quadrupole effects cannot be separated from each other when coherent and directional signals are detected [33]. At first sight, this may appear surprising, because electric and magnetic interactions differ from each other with regard to time-reversal symmetry [32]. However, it is an open question as to how time reversal should be applied to a nonlinear frequency conversion process. This could be approached by considering the reciprocity of the experiment. To do this, another experiment should be performed, where all frequency components, including the ones generated by the sample, are sent back to the sample in reversed order and with proper phase, amplitude and spatial mode, which is clearly beyond experimental capabilities. Just repeating the SHG experiment with front- and back-side incidence is thus not sufficient.

We are thus experimentally limited to spatial symmetry operations. In the effective medium limit, the gradients associated with the quadrupole tensors $\mathbf{A}^{eeQ}$ and $\mathbf{A}^{Qee}$ are related to field propagation, whereas the field components can only involve transverse components. By considering the available spatial symmetry operations, one finds that the quadrupole effects cannot be separated from magnetic effects, as explained in more detail in [33]. From now on, we thus take $\mathbf{A}^{eeQ} = 0$ and $\mathbf{A}^{Qee} = 0$ in equations (1)–(3), with the understanding that the quadrupole effects are implicitly included in the magnetic tensors $\mathbf{A}^{eem}$ and $\mathbf{A}^{mee}$.

We next apply this formalism to the simplest possible geometry, where the incident laser beam is a plane wave propagating along the positive z-direction and is applied at normal incidence on the sample (figure 1).

It is important to note that under the effective-medium assumption, the field components refer to the incident plane waves, not the strongly varying local fields in the nanostructure. The fields thus only have the x- and y-components, also limiting the indices i, j and k in equations (1) and (2) to these values.

The incident plane wave at the fundamental frequency is thus described by

$$\mathbf{E}(\omega) = [\hat{x} E_x(\omega) + \hat{y} E_y(\omega)] \exp[\mathrm{i}(\mathbf{k}_\omega \cdot \mathbf{r} - \omega t)], \tag{4}$$

where $E_x(\omega)$ and $E_y(\omega)$ are the two polarization components of the beam and the wave vector $\mathbf{k}_\omega = (\omega/c)\hat{z}$. From Maxwell's equations, it follows that $\mathrm{i}\mathbf{k}_\omega \times \mathbf{E}(\omega) = \mathrm{i}\omega\mathbf{B}(\omega)$, so that the magnetic and electric field components are related by

$$\begin{pmatrix} B_x(\omega) \\ B_y(\omega) \end{pmatrix} \sim \frac{1}{c} \begin{pmatrix} -E_y(\omega) \\ E_x(\omega) \end{pmatrix}. \tag{5}$$

Once the nonlinear sources have been established, they radiate SHG light according to the emission rules of the electric and magnetic dipole sources [29, 30]. For coherent signals emitted along the sample normal to the reflected and transmitted directions, the SHG signals in the far field are proportional to

$$\mathbf{E}(2\omega) \sim \mathbf{P}(2\omega) + \mathbf{k}_{2\omega} \times \mathbf{M}(2\omega), \tag{6}$$

where $\mathbf{k}_{2\omega}$ is the direction of observation ($\mathbf{k}_{2\omega} = (2\omega/c)\hat{z}$ for transmission or $\mathbf{k}_{2\omega} = -(2\omega/c)\hat{z}$ for reflection).

To understand how the various tensors contribute to possible measured signals, we consider, as an example, the x-polarized SH signal arising from the x-polarized fundamental beam. Within the electric-dipole approximation, the interaction is thus described by the tensor component A_{xxx}^{eee}. We also take the basic geometry to have the fundamental beam incident on the metal side of the sample, which is described by

$$E_x(2\omega) \sim A_{xxx}^{eee} E_x^2(\omega). \tag{7}$$

In the presence of magnetic contributions at the fundamental and SH frequencies, however, this signal is modified by the tensor components A_{xxy}^{eem} and A_{yxx}^{mee}, respectively. By taking these interactions into account and using equations (5) and (6), we find that the transmitted and reflected SH signals, respectively, are of the form

$$E_x(2\omega) \sim \left(A_{xxx}^{eee} + A_{xxy}^{eem} + A_{yxx}^{mee}\right) E_x^2(\omega), \tag{8}$$

$$E_x(2\omega) \sim \left(A_{xxx}^{eee} + A_{xxy}^{eem} - A_{yxx}^{mee}\right) E_x^2(\omega). \tag{9}$$

Note that compared to the basic definitions of equations (1) and (2), all tensors have now been renormalized in a way that all contributions refer to the electric fields at the fundamental and SH frequencies.

The expressions given by equations (8) and (9), however, do not contain sufficient information to determine all the components of the three tensors. Additional information can be obtained by flipping the sample over from metal-side incidence of the fundamental beam to substrate-side incidence. By rotating the sample by 180° about the x-axis (figure 1), and by recalling that under rotations electric and magnetic quantities transform in the same way, any tensor component with odd number of y indices changes sign. For the new geometry, the transmitted and reflected SH signals are thus

$$E_x(2\omega) \sim \left(A_{xxx}^{eee} - A_{xxy}^{eem} - A_{yxx}^{mee}\right) E_x^2(\omega), \tag{10}$$

$$E_x(2\omega) \sim \left(A_{xxx}^{eee} - A_{xxy}^{eem} + A_{yxx}^{mee}\right) E_x^2(\omega). \tag{11}$$

In our experiments, we modulate the polarization of the fundamental beam. We hence have to consider in the same way the electric-dipole tensor components A_{xyy}^{eee} and $A_{xxy}^{eee} = A_{xyx}^{eee}$,

Table 1. NRT element signs with respect to measurement geometry (M-T, metal side, transmission; M-R, metal side, reflection; S-T, substrate side, transmission; S-R, substrate side, reflection).

Geometry	A_{xxx}^{eee}	A_{xxy}^{eem}	A_{yxx}^{mee}	A_{xyy}^{eee}	A_{xyx}^{eem}	A_{yyy}^{mee}	A_{xxy}^{eee}	$(A_{xyy}^{eem} - A_{xxx}^{eem})$	A_{yxy}^{mee}
M-T	+	−	−	+	+	−	−	+	+
M-R	+	−	+	+	+	+	−	+	−
S-T	+	+	+	+	−	+	+	+	+
S-R	+	+	−	+	−	−	+	+	−

and the associated components of the magnetic tensors. The *x*-polarized signal for metal side incidence and transmitted direction is then found to be

$$E_x(2\omega) = \left(A_{xxx}^{eee} + A_{xxy}^{eem} + A_{yxx}^{mee} \right) E_x^2(\omega) + \left(A_{xyy}^{eee} - A_{xyx}^{eem} + A_{yyy}^{mee} \right) E_y^2(\omega)$$
$$+ \left[A_{xxy}^{eee} + \left(A_{xyy}^{eem} - A_{xxx}^{eem} \right) + A_{yxy}^{mee} \right] E_x(\omega) E_y(\omega). \tag{12}$$

In addition, the signs of the various components for the various measured signals are given in table 1. Note that table 1 shows that the tensor components A_{xyy}^{eem} and A_{xxx}^{eem} cannot be separated from each other but can only be measured as the combination $A_{xyy}^{eem} - A_{xxx}^{eem}$.

It is also important to note that absolute signal levels are extremely difficult to calibrate during the measurements. We will therefore take advantage of the fact that the strengths of the various interactions are likely to depend on the state of polarization of the fundamental beam. Our technique is therefore based on manipulating the polarization of the fundamental field continuously while the SH signals are recorded, which leads to varying interference between the different tensor components. Furthermore, the experimentally measured quantities are the irradiances of the SH field. Each measured signal can therefore be fitted to the functional form

$$I_{2\omega} = \left| fE_x^2(\omega) + gE_y^2(\omega) + hE_x(\omega)E_y(\omega) \right|^2, \tag{13}$$

where *f*, *g* and *h* are the fitting parameters expressing the contributions from different quadratic combinations of the polarization components of the fundamental field. It is evident that, except for trivial scaling constants, the parameters are of the form

$$f = A_{xxx}^{eee} \pm A_{xxy}^{eem} \pm A_{yxx}^{mee},$$
$$g = A_{xyy}^{eee} \mp A_{xyx}^{eem} \pm A_{yyy}^{mee}, \tag{14}$$
$$h = A_{xxy}^{eee} \pm \left(A_{xyy}^{eem} - A_{xxx}^{eem} \right) \pm A_{yxy}^{mee},$$

where the proper signs for each signal are given in table 1.

By measuring and analyzing all the four signals, we therefore obtain various combinations of the tensor components. The results can thus be used to construct a group of linear equations, where the unknowns are the tensor components and arbitrary scaling constants between the four signals. In the present case, the measured results provide a sufficient number of independent parameters that allow all of the unknowns to be uniquely determined.
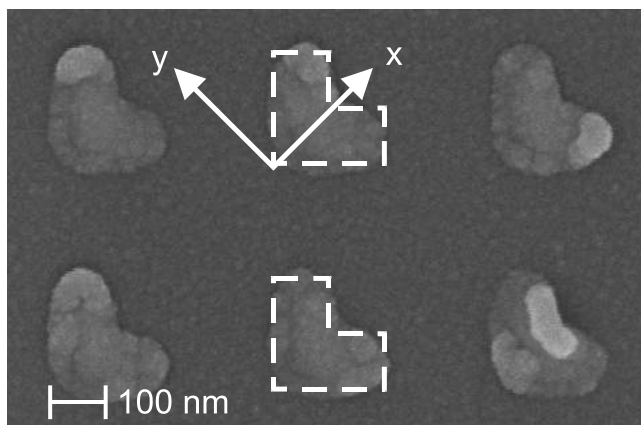
Figure 2. Scanning electron micrograph of the sample with the principal axes marked.

3. Experimental methods

Our sample consisted of an array of L-shaped gold nanoparticles. The linewidth of the particle arms is about 100 nm, the arm length is about 200 nm and the thickness of the metal layer is about 20 nm. The particles are ordered in a square lattice with a 400 nm period. The sample is covered with a 20 nm thick protective layer of silica. The active area of the sample is 1 mm × 1 mm. A scanning electron micrograph of the sample is shown in figure 2. The nanoparticles were deposited on a silica glass substrate using standard electron-beam lithography and the lift-off process [37].

The symmetry of an ideal L-shaped particle with equal arm lengths dictates a natural coordinate system for the sample. The principal axes denoted as x and y are rotated by 45° relative to the electron-beam lithography writing system. For the case of ideal, symmetric particles, the x-axis is a mirror symmetry axis. Reflection with respect to this axis is the only symmetry operation for the sample. However, in the case of a real structure, the symmetry is broken due to shape distortions from the ideal and by the surface defects. The ideal geometrical L outline in figure 2 emphasizes the deviation of the real sample from the ideal. The sample exhibits strong dichroism [38], with x- and y-polarizations having well-defined plasmonic resonances at the wavelengths of about 1050 and 1500 nm, respectively.

The experiments were performed using a femtosecond Nd:glass laser (200 fs pulse length, 82 MHz repetition rate and 320 mW average power) as the source of fundamental light (figure 3). The x-polarization plasmonic resonance is thus close to the laser wavelength of 1060 nm. In addition, for the x-polarized fundamental beam, the x-polarized SH signal, described by the tensor component A_{xxx}^{eee}, is electric-dipole-allowed by the ideal structural symmetry of the sample. Focusing the present study on the x-polarized SH signals is therefore particularly relevant for demonstrating the capabilities of our new measurement technique in addressing the interplay of plasmon resonances and various multipole effects in the nonlinear response of the sample.

The laser light is weakly focused on the sample (spot size about 200 μm). The state of polarization of the fundamental beam is controlled with a polarizer P1 (cf figure 3), passing the linear p-polarization (in the plane of incidence). During the measurements, the
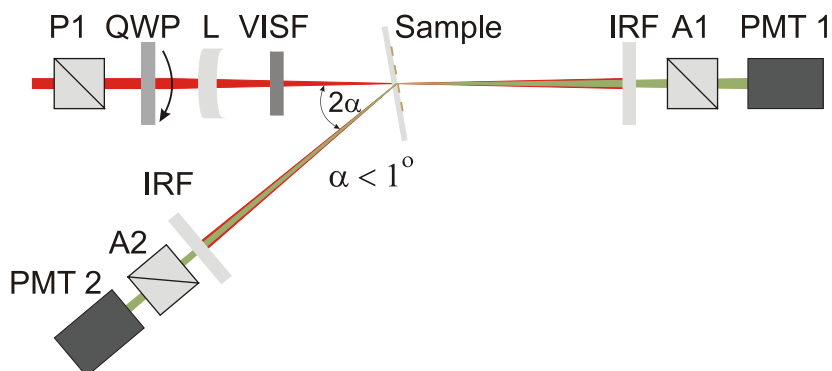
Figure 3. Experimental setup (VISF, visible blocking filter; IRF, infrared blocking filters; PMT 1, 2, photomultiplier tubes; P1, polarizer; A1, A2, analyzers).

state of polarization is modulated continuously with a quarter-wave plate (QWP), mounted in a computer-controlled, motorized rotation stage. Due to simultaneous measurements of the transmitted and reflected SHG signals, the sample is slightly (around 1°) tilted off normal with respect to the fundamental beam. We have performed several tests to verify that this angle is sufficiently small to make the coupling of the fields with the sample normal direction (z) insignificant [30, 31]. The s- and p-polarization components can thus be equated with the x- and y-polarizations, respectively.

The generated SHG light passes through an s-directed (normal to the plane of incidence) analyzer. The s-polarized SH signal is thus detected as a function of the fundamental beam polarization state controlled with the QWP rotation angle. The SHG signal is detected with a sensitive photomultiplier tube connected to a photon counting system. To make sure that the measured signal is SHG light and that it originates from the sample itself, visible and infrared blocking filters were used before and after the sample, respectively. The measurements were repeated for both orientations (metal and substrate side incidence) of the sample in the setup.

4. Results and discussion

The four measured signals as functions of the rotation angle of the QWP and their fits to equation (13) are shown in figure 4. In order to address whether an electric-dipole-only model could explain the data, the polarization lineshapes for the substrate-side incidence data have been reflected with respect to zero angle of the wave plate. This is because the change in the orientation of the sample reverses the sign of the y-coordinate of the sample, and hence this must be taken into account in describing how the wave plate modulates the state of polarization in the sample frame of reference (see also table 1). After this detail has been taken into account, all measured lineshapes would have to be identical if only electric dipoles were present.

The results of figure 4 have several interesting features. First, the overall features of all four lineshapes are very similar to each other, which would suggest that electric-dipole effects dominate the response. However, the lineshapes do have significant differences with regard to their details, both between the reflected and transmitted SHG signals and between the SHG signals for the metal and substrate side incidence of the fundamental beam. These
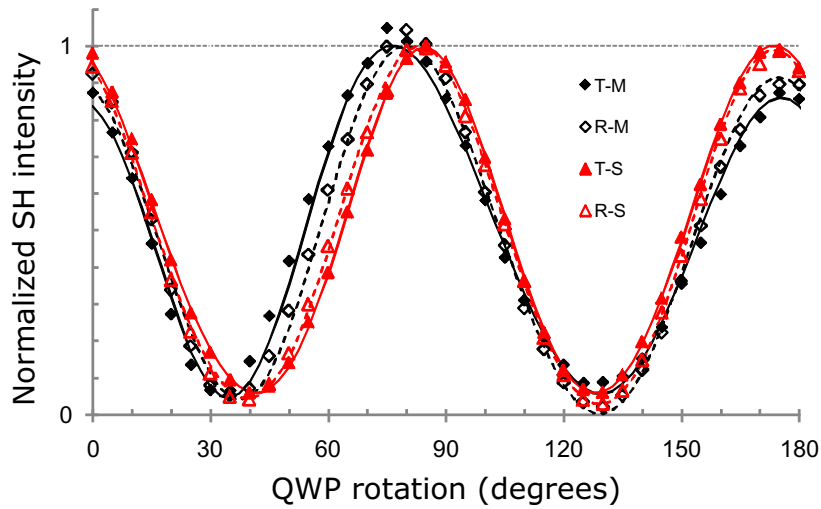
Figure 4. Comparison of data sets for different geometries of the measurement and their fits to the model of equation (13). The labels refer to transmission (T), reflection (R), metal incidence (M) and substrate incidence (S). Note that the results for the metal incidence are plotted from $0°$ to $-180°$, instead of $0°$ to $180°$, to account for the change in sign of the y-coordinate between the two geometries.

Table 2. Results for the fits to equation (14). The error for all obtained values was estimated to be smaller than 0.03 units for both the real and imaginary parts.

NRT element	Value	Magnitude
A_{xxx}^{eee}	1	1
A_{xxy}^{eem}	$-0.239 + 0.408i$	0.473
A_{yxx}^{mee}	$0.034 + 0.041i$	0.054
A_{xyy}^{eee}	$0.794 + 0.063i$	0.797
A_{xyx}^{eem}	$0.233 - 0.315i$	0.392
A_{yyy}^{mee}	$0.012 - 0.033i$	0.035
A_{xxy}^{eee}	$0.199 - 0.086i$	0.217
$(A_{xyy}^{eem} - A_{xxx}^{eem})$	$0.438 + 0.137i$	0.459
A_{yxy}^{mee}	$0.003 + 0.007i$	0.007

differences already provide qualitative evidence of the importance of higher multipole effects at the fundamental and SH frequencies.

In order to obtain more quantitative information about the importance of the higher multipole effects, the fit parameters f, g and h for each measured signal were expressed in terms of the components of the tensors to set up a group of linear equations with the tensor components and scaling constants of the signals as unknowns. The solution is shown in table 2, where the values have been normalized to the electric-dipole-allowed component A_{xxx}^{eee}. The error for all obtained values was estimated to be smaller than 0.03 unit for both the real and the imaginary parts. Note that this component is electric-dipole-allowed for the ideal structure and

corresponds to the case where the fundamental wavelength is close to the plasmon resonance of this polarization. This component is indeed found to dominate the response. However, the other electric-dipole-allowed component A_{xyy}^{eee} is almost as large in magnitude, whereas the ideally forbidden component A_{xxy}^{eee} is significantly smaller.

The results also show that the higher multipole effects are much stronger in tensor A_{ijk}^{eem} than in tensor A_{ijk}^{mee}. The higher multipole effects are thus significantly more important at the fundamental frequency than at the SH frequency. This result is an important difference compared to our earlier results [30, 31], where the multipole effects were explained in terms of different radiative properties of the various multipoles, i.e. assuming that all multipole effects occur at the SH frequency. This new result could only be obtained by our new technique, where the sample is characterized in two different orientations (metal and substrate side incidence). The importance of higher multipole effects at the fundamental frequency is likely related to the fact that the particles support plasmonic resonances and thus strong local fields only at the fundamental frequency but not at the SH frequency. The field gradients favorable for the multipole effects are therefore stronger at the fundamental frequency.

It is also interesting to compare the relative importance of the higher multipole effects to the various measured signals. The electric-dipole-allowed resonant signal, which arises from the tensor components A_{xxx}^{eee}, A_{xxy}^{eem} and A_{yxx}^{mee}, is clearly dominated by electric-dipole effects, although higher multipoles also make a significant contribution. The same applies to the allowed signal due to A_{xyy}^{eee}, A_{xyx}^{eem} and A_{yyy}^{mee}. However, the forbidden signal, due to the components A_{xxy}^{eee}, $A_{xyy}^{eem} - A_{xxx}^{eem}$ and A_{yxy}^{mee}, which can only arise from sample imperfections (such as shape deviations from ideal and nanoscale defects), is dominated by the higher multipole components. This is in agreement with the earlier interpretation that higher multipole effects are associated with symmetry-breaking surface defects and field retardation [30, 31]. On the other hand, the role of higher multipole effects in the allowed signals suggests that not all surface defects need to break the symmetry and thus only contribute to retarded wavelets.

5. Conclusions

In conclusion, we have presented a new measurement technique that allows the role of the electric-dipole and higher-multipole contributions to the SH response of metal nanostructures to be addressed in detail. The technique is based on the effective medium approach where a total of three effective nonlinear response tensors are introduced to account for the electric-dipole interactions and the magnetic-dipole interactions to lowest-order at the fundamental and SH frequencies. The technique is based on the different transformation properties of the three tensors as the experimental geometry is manipulated. In particular, comparison of the SH signals emitted in the reflected and transmitted directions provides evidence of higher-multipole effects at the SH frequency [30, 31], whereas comparison of the signals for the fundamental beam incident on the metal and substrate sides provides complementary information that can be correlated with the presence of higher multiple effects at the fundamental frequency.

The present results show that the four measured signals have important differences in their details. The results for the sample investigated suggest that the dipolar response dominates; however, significant effects beyond electric dipoles are also present. Furthermore, the higher multipole effects are significantly more important at the fundamental frequency than at the SH frequency. In addition, the signal that is electric-dipole-forbidden for the ideal structure

is dominated by the higher multipole effects. This provides further support to the interpretation that the higher multipole effects are closely related to the surface defects of the sample. In the future, it will be interesting to investigate the role of the multipole effects under resonant and non-resonant excitation and for samples with varying surface quality.

Acknowledgments

References

[1] Kreibig U and Vollmer M 1995 *Optical Properties of Metal Clusters* (*Springer Series in Material Science*) (Berlin: Springer)
[2] Tsang T Y F 1996 Surface-plasmon-enchanced third-harmonic generation in thin silver films *Opt. Lett.* **21** 245
[3] Félidj N, Aubard J, Lévi G, Krenn J R, Salerno M, Schider G, Lamprecht B, Leitner A and Aussenegg F R 2002 Controlling the optical response of regular arrays of gold particles for surface-enhanced Raman scattering *Phys. Rev.* B **65** 075419
[4] Bouhelier A, Beversluis M, Hartschuh A and Novotny L 2003 Near-field second-harmonic generation induced by local field enhancement *Phys. Rev. Lett.* **90** 013903
[5] Stockman M I, Bergman D J and Kobayashi T 2004 Coherent control of nanoscale localization of ultrafast optical excitation in nanosystems *Phys. Rev.* B **69** 054202
[6] Shalaev V M, Poliakov E Y and Markel V A 1996 Small-particle composites. II. Nonlinear optical properties *Phys. Rev.* B **53** 2437–449
[7] Guyot-Sionnest P, Chen W and Shen Y 1986 General considerations on optical second-harmonic generation from surfaces and interfaces *Phys. Rev.* B **33** 8254
[8] Dadap J I, Shan J, Eisenthal K B and Heinz T F 1999 Second-harmonic Rayleigh scattering from a sphere of centrosymmetric material *Phys. Rev. Lett.* **83** 4045
[9] Dadap J I, Shan J and Heinz T F 2004 Theory of optical second-harmonic generation from a sphere of centrosymmetric material: small-particle limit *J. Opt. Soc. Am.* B **21** 1328–47
[10] Shan J, Dadap J I, Stiopkin I, Reider G A and Heinz T F 2006 Experimental study of optical second-harmonic scattering from spherical nanoparticles *Phys. Rev.* A **73** 023819
[11] Loudon R 1983 *The Quantum Theory of Light* 2nd edn (New York: Oxford University Press)
[12] Bachelier G, Russier-Antoine I, Benichou E, Jonin C and Brevet P-F 2008 Multipolar second-harmonic generation in noble metal nanoparticles *J. Opt. Soc. Am.* B **25** 955
[13] Kauranen M, Verbiest T, Maki J J and Persoons A 1994 Second-harmonic generation from chiral surfaces *J. Chem. Phys.* **101** 8193
[14] Kauranen M, Maki J J, Verbiest T, Elshocht S V and Persoons A 1997 Quantitive determination of electric and magnetic second-order susceptibility tensors of chiral surfaces *Phys. Rev.* B **55** R1985
[15] Elshocht S V, Verbiest T, Kauranen M, Persoons A, Langeveld-Voss B M W and Meijer E W 1997 Direct evidence of the failure of electric-dipole approximation in second-harmonic generation from a chiral polymer film *J. Chem. Phys.* **107** 8201
[16] Schanne-Klein M C, Hache F, Brotin T, Andraud C and Collet A 2001 Magnetic chiroptical effects in surface second-harmonic reflection *Chem. Phys. Lett.* **338** 159

[17] Oldenburg S J, Hale G D, Jackson J B and Halas N J 1999 Light scattering from dipole and quadrupole nanoshell antennas *Appl. Phys. Lett.* **75** 1063

[18] Kelly K L, Coronado E, Zhao L L and Schatz G C 2003 The optical properties of metal nanoparticles: the influence of size, shape, and dielectric environment *J. Phys. Chem.* B **107** 668

[19] Petschulat J, Menzel C, Chipouline A, Rockstuhl C, Tünnermann A, Lederer F and Pertsch T 2008 Multipole approach to metamaterials *Phys. Rev.* A **78** 043811

[20] Belardini A, Larciprete M C, Centini M, Fazio E, Sibilia C, Bertolotti M, Toma A, Chiappe D and Buatier de Mongeot F 2009 Tailored second harmonic generation from self-organized metal nano-wires arrays *Opt. Express* **17** 3603

[21] Krenn J, Schider G, Rechberger W, Lamprecht B, Leitner F, Aussenegg A and Weeber J 2000 Design of multipolar plasmon excitations in silver nanoparticles *Appl. Phys. Lett.* **77** 3379–81

[22] Klein M W, Enrich C, Wegener M and Linden S 2006 Second-harmonic generation from magnetic metamaterials *Science* **313** 502–4

[23] Cho D J, Wang F, Zhang X and Shen Y R 2008 Contribution of the electric quadrupole resonance in optical metamaterials *Phys. Rev.* B **78** 121101

[24] Brudny V L, Mochán W L, Maytorena J A and Mendoza B S 2003 Second harmonic generation from a collection of nanoparticles *Phys. Status Solidi* b **240** 518–28

[25] Valencia C I, Méndez E R and Mendoza B S 2003 Second-harmonic generation in the scattering of light by two-dimensional particles *J. Opt. Soc. Am.* B **20** 2150–61

[26] Nappa J, Revillod G, Russier-Antoine I, Benichou E, Jonin C and Brevet P F 2005 Electric dipole origin of the second harmonic generation of small metallic particles *Phys. Rev.* B **71** 165407

[27] Nappa J, Russier-Antoine I, Benichou E, Jonin C and Brevet P F 2006 Second harmonic generation from small gold particles: from the dipolar to the quadrupolar response *J. Chem. Phys.* **125** 184712

[28] Petschulat J, Chipouline A, Tünnermann A, Pertsch T, Menzel C, Rockstuhl C and Lederer F 2009 Multipole nonlinearity of metamaterials *Phys. Rev.* A **80** 063828

[29] Butet J, Duboisset J, Bachelier G, Russier-Antoine I, Benichou E, Jonin C and Brevet P-F 2010 Second harmonic generation of single metallic nanoparticles embedded in a homogeneous medium *Nano Lett.* **10** 1717

[30] Kujala S, Canfield B K, Kauranen M, Svirko Y and Turunen J 2007 Multipole interference in the second-harmonic optical radiation from gold nanoparticles *Phys. Rev. Lett.* **98** 167403

[31] Kujala S, Canfield B K, Kauranen M, Svirko Y and Turunen J 2008 Multipolar analysis of second-harmonic radiation from gold nanoparticles *Opt. Express* **16** 17196

[32] Jackson J 1975 *Classical Electrodynamics* 2nd edn (New York: Wiley)

[33] Kauranen M, Verbiest T and Persoons A 1998 Second-order nonlinear optical signatures of surface chirality *J. Mod. Opt.* **45** 403

[34] Bai B and Turunen J 2007 Fourier modal method for the analysis of second-harmonic generation in two-dimensionally periodic structures containing anisotropic materials *J. Opt. Soc. Am.* B **24** 1105

[35] Canfield B K, Kujala S, Jefimovs K, Svirko Y, Turunen J and Kauranen M 2006 A macroscopic formalism to describe the second-order nonlinear optical response of nanostructures *J. Opt.* A **8** 278–84

[36] Pershan P 1963 Nonlinear optical properties of solids: energy considerations *Phys. Rev.* **130** 919

[37] Tuovinen H, Kauranen M, Jefimovs K, Vahimaa P, Vallius T, Turunen J, Tkachenko N V and Lemmetyinen H 2002 Linear and second-order nonlinear optical properties of arrays of noncentrosymmetric gold nanoparticles *J. Nonlinear Opt. Phys. Mater.* **11** 421

[38] Canfield B K, Kujala S, Laiho K, Jefimovs K, Turunen J and Kauranen M 2006 Chirality arising from small defects in gold nanoparticle arrays *Opt. Express* **14** 950–5